Ultrafast laser-scanning optical resolution photoacoustic microscopy at up to 2 million A-lines per second

Thomas John Allen
Josh Spurrell
Martin O. Berendt
Olumide Ogunlade
Shaif U. Alam
Edward Z. Zhang
David J. Richardson
Paul C. Beard

Ultrafast laser-scanning optical resolution photoacoustic microscopy at up to 2 million A-lines per second

Thomas John Allen,[a,][*] Josh Spurrell,[b] Martin O. Berendt,[b] Olumide Ogunlade,[a] Shaif U. Alam,[b] Edward Z. Zhang,[a] David J. Richardson,[b] and Paul C. Beard[a]
[a]University College London, Department of Medical Physics and Biomedical Engineering, London, United Kingdom
[b]University of Southampton, Optoelectronics Research Centre, Southampton, United Kingdom

Abstract. The imaging speed of optical resolution photoacoustic microscopy (OR-PAM) using pulsed excitation is fundamentally limited by the range ambiguity condition, which defines the maximum laser pulse repetition frequency (PRF). To operate at this theoretical upper limit and maximize acquisition speed, a custom-built fiber laser capable of operating at a PRF of up to 2 MHz was combined with a fast laser scanning optical OR-PAM system based on a stationary fiber-optic ultrasound sensor. A large area (10 mm × 10 mm) of the mouse ear was imaged within 8 s, when acquiring 16 million A-lines and operating the laser at a PRF of 2 MHz. This corresponds to a factor of four improvement in imaging speed compared to the fastest OR-PAM system previously reported. The ability to operate at high-imaging frame rates also allows the capture of hemodynamic events such as blood flow. It is considered that this system offers opportunities for high throughput imaging and visualizing dynamic physiological events using OR-PAM. © *The Authors. Published by SPIE under a Creative Commons Attribution 3.0 Unported License. Distribution or reproduction of this work in whole or in part requires full attribution of the original publication, including its DOI.* [DOI: 10.1117/1.JBO.23.12.126502]

Keywords: optical resolution photoacoustic microscopy; fiber laser; microscopy.

Paper 180500R received Aug. 15, 2018; accepted for publication Oct. 26, 2018; published online Dec. 6, 2018.

1 Introduction

Optical resolution photoacoustic microscopy (OR-PAM) can provide high-resolution ($<10~\mu$m) absorption-based images to sub-mm penetration depths.[1–3] These images are usually formed by raster scanning a pulsed focused laser beam relative to the tissue surface and detecting the generated time-resolved photoacoustic signals at each scan point. The imaging speed is determined by the rate at which A-lines can be acquired which is fundamentally limited by the range-ambiguity (RA) condition. This requires that the time separation between two consecutive laser pulses is sufficiently long that the photoacoustic waves generated by the first laser pulse arrive at the tissue surface before the second pulse is delivered. For example, for an absorber located at a depth of 750 μm (a depth rarely exceeded in OR-PAM) and assuming a sound speed of 1485 m/s, the acoustic propagation time to the surface is $\sim$0.5 μs; under these conditions, the maximum RA limited pulse repetition frequency (PRF) is, therefore, 2 MHz. To date, no OR-PAM system that can operate at this theoretical limit has been reported. In some cases, this is because an excitation laser source with an insufficiently high PRF was employed. In others, a laser with a high enough PRF was used but the OR-PAM scanner employed was insufficiently fast to exploit the high PRF of the laser. That is to say, the scanner could not displace the excitation beam relative to the sample (or vice-versa) sufficiently far (e.g., on the order of half the focal spot size) between the firing of two consecutive excitation laser pulses to interrogate spatially distinct points.

With respect to the excitation laser, diode pumped solid-state lasers have been widely used in OR-PAM[1,4] as they provide the necessary short pulse duration ($<$2 ns) and adequate pulse energies (in the range 100 nJ to 10 μJ). They can also operate at visible wavelengths, when frequency doubled or combined with a dye laser[1,5] or a photonic crystal fiber.[6] However, their PRFs are typically limited to the tens of kHz range resulting in acquisition rates that are at least an order of magnitude lower than dictated by the RA condition. To overcome this limitation, fiber lasers have been used in OR-PAM,[7–12] as they can readily provide PRFs in the hundreds of kilohertz to low megahertz range while fulfilling the requirements for a high-quality beam, short-pulse duration, and microjoule pulse energies. However, none of these previous fiber laser-based OR-PAM systems provided RA limited acquisition rates—the highest acquisition speed was provided by a system based on a submersible 1-D MEMs-based scanner.[11] This could scan sufficiently rapidly to exploit PRFs up to 500 kHz but this is still significantly below the 2-MHz RA limited PRF referred to above. The use of a fiber laser that could provide PRFs up to 2 MHz has also been reported for OR-PAM.[13] However, this system employed mechanical scanning implemented using motorised translation stages, which were too slow to exploit the high PRF of the laser. As a consequence, the reported acquisition speed was at least two orders of magnitude below the RA limit.

In this study, we describe an OR-PAM system that can overcome the above limitations and provide an RA limited acquisition speed that is at least a factor of 4 higher than any previously reported OR-PAM scanner. This is achieved by combining two key components: a custom fiber laser that can operate at a PRF up to 2 MHz and an OR-PAM scanner that is fast enough to exploit this high PRF. The latter is achieved using a fast galvanometer-based scanner to raster scan the laser beam over the

---

*Address all correspondence to: Thomas John Allen, E-mail: t.allen@ucl.ac.uk

sample surface and a static fiber-optic ultrasound detector to record the acoustic signals.[14] Using a stationary detector in this way, and thereby avoiding the time penalties associated with mechanical sample/detector scanning, an A-line rate limited only by the galvanometer speed can be achieved. As we show, this is sufficiently high to exploit the 2-MHz PRF of the fiber excitation laser and provide true RA limited OR-PAM acquisition rates for the first time.

A preliminary study[15] has demonstrated this concept by imaging phantoms composed of highly optically absorbing features. In the current study, we demonstrate the acquisition of *in vivo* images over large areas while operating at acquisition rates of up to 2 million A-lines per second. For example, an image of the microvasculature of a mouse ear composed of 16 million A-lines was obtained in just 8 s when imaging a 10 mm × 10 mm area. In addition, the ability to image hemodynamic events in real time over smaller areas is demonstrated.

Section 2 describes the experimental setup. Section 3.1 demonstrates the ability of the system to rapidly acquire static *in vivo* images of the mouse ear microvasculature in forward and backward modes, whereas Sec. 3.2 demonstrates the ability of the system to acquire dynamic images.

2 Laser Scanning OR-PAM Setup

The experimental setup is shown in Fig. 1. It is based on a laser scanning OR-PAM configuration, in which a focussed excitation beam is optically scanned across the sample and the photoacoustic waves generated at each point are detected by a stationary fiber-optic ultrasound receiver. As we show, this approach enables unprecedentedly high OR-PAM image frame rates limited by the RA condition, which sets the theoretical upper limit in terms of acquisition speed. The system comprises three key components: (i) a custom-built fiber excitation laser that can operate at a PRF of up to 2 MHz, (ii) a fast
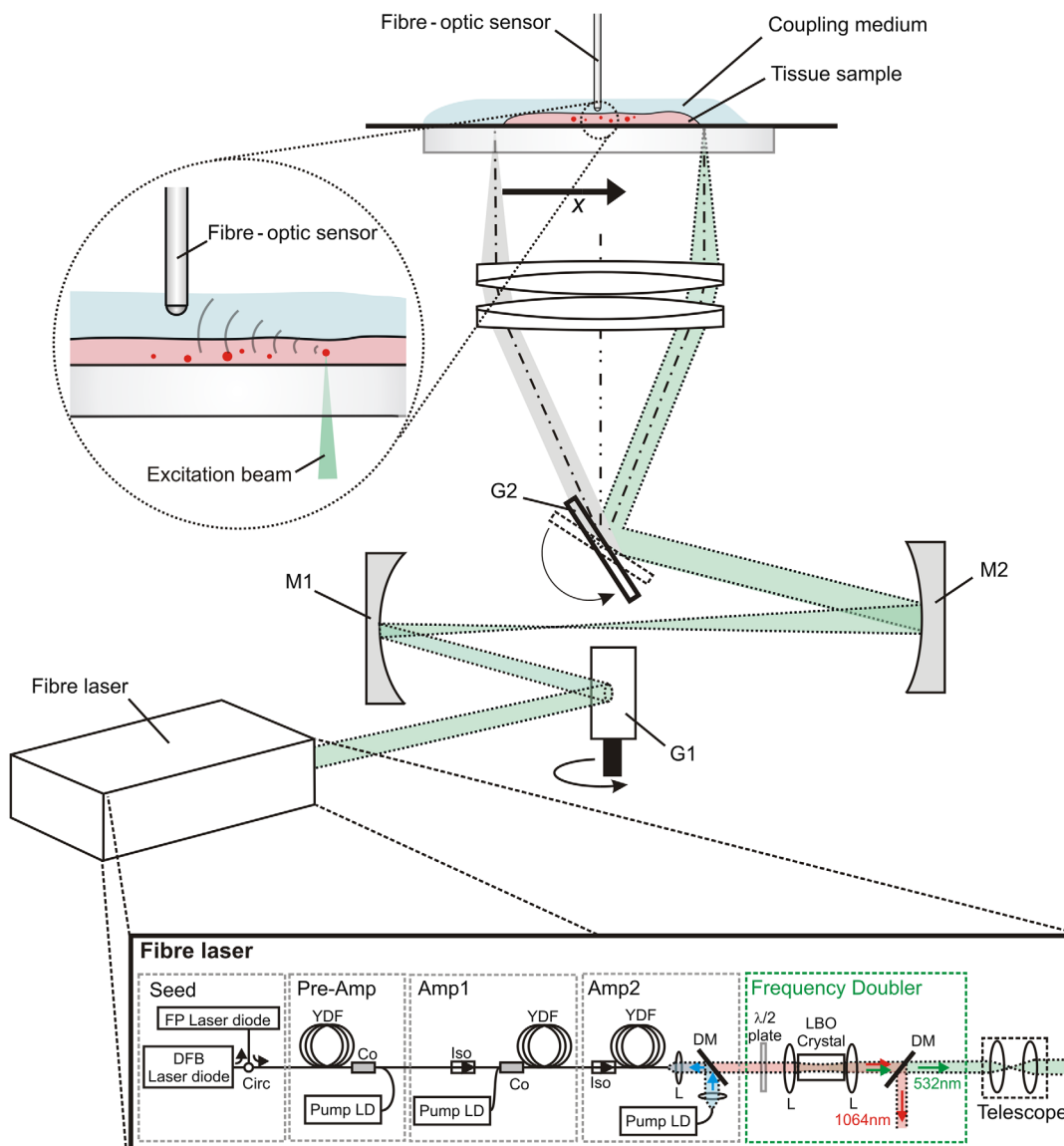

Fig. 1 Experimental laser scanning OR-PAM setup. G1 and G2, first and second galvanometer mirrors; M1 and M2, first and second concave mirrors; LD, laser diode; YDF, Yb-doped fiber; DM, dichroic mirror; L, lens; Iso, isolator; Co, coupler; Circ, circulator; and M, mirror. The FWHM of the focal spot on the sample was 7 μm and the maximum scan area was 10 mm × 10 mm.

galvanometer based $x - y$ optical scanner, and (iii) a highly sensitive broadband near-omnidirectional fiber-optic ultrasound detector. Each of these is discussed in turn below.

2.1 Fiber Laser Excitation System

The design of the fiber laser was based on a master oscillator power amplifier (MOPA) configuration, operating at an emission wavelength of 1064 nm, which was then frequency doubled to 532 nm. The MOPA consisted of a seed laser, one preamplifier stage, and two high-power fiber amplifiers (see inset of Fig. 1). Polarization maintaining fiber was used throughout in order to provide a linearly polarized output as required for the final stage frequency doubling. The seed laser comprised a Fabry-Pérot laser diode that was injection locked using a distributed feedback laser diode in order to provide relatively high peak powers (> 100 mW) and a narrow linewidth (<0.7 nm). The latter is required for efficient second harmonic generation (SHG). The output of the seed laser was amplified by the preamplifier, which comprised a 6-m long Ytterbium-doped fiber with a 6-μm core diameter that was core-pumped using a 978-nm CW single-mode laser diode in a backward configuration. The first high-power amplifier stage (Amp1) used a 6-m long Ytterbium-doped fiber with a 10-μm core diameter and was cladding-pumped using a 915-nm CW laser diode in a forward configuration. Cladding pumping allows the use of high-power multimode laser diodes whose poor beam quality does not permit efficient launching into a single-mode core. The second high-power amplifier stage (Amp 2) used a 3-m long Ytterbium-doped fiber with a 25-μm core diameter and was cladding-pumped using a 975-nm CW laser diode and free space optics in a backward configuration. Using a large core diameter (25 μm) fiber increases the power handling of the amplifier and the threshold for nonlinear effects. To ensure that only the fundamental mode propagated within the fiber, it was coiled around a 70-mm diameter cylinder, causing the higher order modes to leak out of the core. The output of the laser was then frequency doubled using a lithium triborate (LBO) nonlinear crystal. To achieve this, the beam was passed through a half wave plate to rotate the polarization of the light to match the optical axis of the crystal. The beam is then passed through a lens in order to focus it within the LBO crystal for SHG. The LBO crystal has a length of 25 mm and phase matching was implemented by tuning its temperature to 154°C. The second harmonic beam was collimated and separated from the residual fundamental beam after reflection from a dichroic mirror.

The system provided a PRF that was variable between 250 kHz and 2 MHz, a minimum pulse energy of 0.5 μJ at the laser output, pulse duration of 1.4 ns, and a high beam quality ($M^2 < 1.12$). The laser was designed to operate at a maximum PRF of 2 MHz, which corresponds to an RA limited maximum penetration depth of 750 μm.

2.2 Optical Scanning System

The scanning system is based on an asymmetric conjugate scanner specifically designed to provide both high speed and large field-of-view (FOV). The system comprises a pair of mutually orthogonal $x - y$ galvanometers (G1 and G2, Cambridge Technology Ltd.), which are used to raster scan the excitation beam over a pair of achromatic lenses (AC508-100-A, Thorlabs Ltd.) that focus the beam on to the sample; the focal length of

the achromatic pair was 5 cm. The scanner has several specific design features. First, the collimated beam emitted by the laser is scanned by G1 over the surface of two off-axis concave mirrors (M1 and M2) and subsequently directed to a single point on G2. Rotation of G1, therefore, rotates the beam about a spatially invariant pivot-point on G2 thereby avoiding any beam shift, which would otherwise distort the focal spot, particularly when the beam is off-axis, which limits the FOV. Second, the focal lengths of the concave mirrors (M1 and M2) were chosen to be 5 and 10 cm, respectively, resulting in the initial 3-mm diameter beam provided by the fiber laser being expanded to twice its original diameter following its reflection from M2. This arrangement offers two advantages. First, the excitation beam that is incident on the achromatic doublet is of large diameter (⌀6 mm). This enables a reasonably small focal spot of 7-μm diameter (FWHM)[5,14] to be achieved using a scan lens with a relatively long focal length so as to provide a large FOV (>10 mm $\times$ 10 mm) with minimal vignetting. Second, using M1 and M2 to expand the beam diameter downstream of G1 means that the dimensions of G1 can be kept small (5 mm $\times$ 5 mm). This minimizes inertia and thus maximizes speed, an important requirement for G1 since it provides scanning along the fast axis. By contrast, G2 is the slow-axis scanning galvanometer. Hence, a relatively large mirror (10 mm $\times$ 15 mm) can be tolerated in order to accommodate the expanded 6-mm diameter beam reflected from M2.

The galvanometers were driven with a triangular waveform, continually scanning them back and forth. The oscillation frequency of the small mirror (G1) can reach 1 kHz depending on the scanning angles required. For example, when scanning over an angle of 1.4 deg, equivalent to a displacement of 1.25 mm on the tissue surface, the scanning speed of the mirror can be set to 1 kHz, corresponding to 2000 B-scans per second.

2.3 Acoustic Detection and Signal Acquisition

The generated photoacoustic signals were detected using a planoconcave fiber-optic sensor that was acoustically coupled to the tissue sample using ultrasound gel. The design and acoustic performance of the sensor has been described previously.[16,17] Briefly, it comprised a 33.1-μm-thick planoconcave polymer cavity that acts as an optical microresonator deposited on to the tip of a single-mode fiber with a 10-μm core diameter. An incident acoustic wave modulates the optical thickness of the cavity and thus its reflectivity. This is read-out using a CW 1550-nm laser beam that is coupled into the core of the fiber and tuned to a wavelength that corresponds to the edge of the cavity resonance. The sensor provides a high detection sensitivity (NEP < 0.1 kPa over a 20-MHz measurement bandwidth[16]) and a broad bandwidth that extends to 60 MHz. An important characteristic of the sensor is the large acoustic acceptance angle (± 90 deg) it provides due to its small active element size (~10 μm).[16,17] As a consequence, it provides a near omnidirectional response enabling photoacoustic waves generated over a large lateral FOV to be recorded without translating the sensor.

The photoacoustic signals recorded at each scan position were continuously streamed to a PC via a fast digitising card (PCI-5114 National Instruments) with a sampling rate of 50 MS/s and 8-bit resolution. A fast photodiode connected to the second channel of the digitizer was used to monitor the excitation laser pulses and remove any timing uncertainty due to jitter. To form an image, a maximum intensity projection (denoted $\text{MIP}_{\text{pk-pk}}$) was produced by plotting the peak-to-peak

amplitudes extracted from each recorded photoacoustic waveform as a function of x–y position.

3 In Vivo Imaging of Mouse Ear Microvasculature

3.1 Static Image Acquisition

As an initial evaluation of the system, and in order to provide a reference image to which subsequent images obtained when operating at a PRF of 2 MHz could be compared, the ear of a nude mouse was imaged while operating at 500 kHz PRF. The mouse was anaesthetized using a mixture of isoflorane and oxygen at a concentration of 4% for induction, and 1% to 2% for maintenance, with flow rates of 1 l/min. All experiments were performed in accordance with the UK Home Office Animals Scientific Procedures Act (1986). Images were acquired in both forward and backward modes. Figure 2(a) shows a schematic depicting the position of the sensor when operating in forward mode, and Fig. 2(b) shows the corresponding photoacoustic image of the mouse ear displayed as an

MIP$_{pk-pk}$. The imaged area was 8 mm × 13 mm with 2- and 3.25-μm step sizes in the x and y directions, respectively. At each scan point, a single A-line was acquired, thus a total of $N = 16$ million A-lines were recorded. The acquisition time was 32 s and was limited by the PRF of the laser (500 kHz). The pulse energy of the fiber laser was 500 nJ, corresponding to an estimated fluence at the focus of 1.3 J/cm^2, which is comparable to that used in previous OR-PAM studies.[2,18–20] The microvasculature down to the level of individual capillaries can be clearly visualized with high contrast as shown in Fig. 2(b).

Figure 2(c) shows a schematic depicting the position of the sensor when operating in backward mode, which allows images to be acquired when access to both sides of the tissue is unavailable. The sensor was embedded in the substrate, by creating a groove in the substrate at a 30-deg angle where the sensor was placed. Figure 2(d) shows the acquired photoacoustic image of the mouse ear. As with the forward mode configuration, the microvasculature at the capillary level can be visualized. The imaging parameters were identical to those used in forward mode; other than the pulse energy was increased to 900 nJ to compensate for the greater acoustic propagation distance in
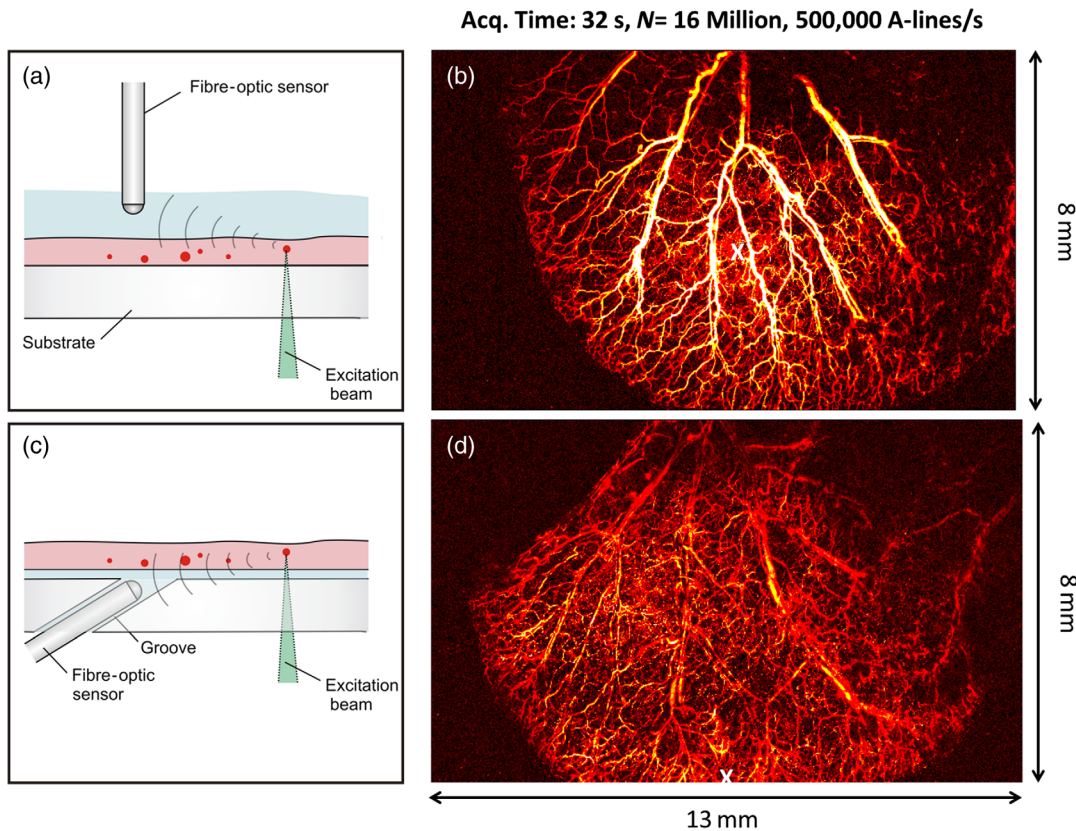

Acq. Time: 32 s, N= 16 Million, 500,000 A-lines/s

Fig. 2 Photoacoustic imaging of a mouse ear in forward and backward modes at 500,000 A-lines/s. (a) Schematic showing the position of the fiber-optic sensor when imaging in forward mode, (b) photoacoustic image obtained *in vivo* of a mouse ear while operating in forward mode, (c) schematic showing the position of the fiber-optic sensor when imaging in backward mode, and (d) photoacoustic image obtained *in vivo* of a mouse ear when operating in backward mode. In both cases, the scan area was 8 mm × 13 mm with 2- and 3.25-μm step size in the x and y directions, respectively, and the total number of A-lines acquired was $N = 16$ million. The x and y galvanometers were driven at 62.5 and 0.015625 Hz, respectively. The PRF of the laser was 500 kHz and the pulse energy was 500 and 900 nJ for the forward and backward mode configurations, respectively. The position of the fiber sensor is indicated by the white cross in (b) and (d) and was located 1.5 mm above the sample for the forward mode configuration and directly adjacent to the sample for the backward mode configuration.

the backward mode configuration compared to forward mode configuration.

Following the above initial evaluation of the system, the highest possible acquisition speed was achieved by increasing the PRF in order to acquire A-lines at a rate of 2 million per second. To achieve this, an area of 10 mm × 10 mm was imaged in forward mode when operating the fiber laser at a PRF of 2 MHz, which corresponds to an RA limited depth of 750 μm. The acquired photoacoustic image is shown in Fig. 3 and is of comparable quality to the images in Fig. 2. The photoacoustic image was formed of 16 million A-lines, which were acquired in 8 s, representing a factor of 4 increase in imaging speed compared to the imaging speed achieved in Figs. 2(b) and 2(d). Imaging in backward mode was not attempted at a PRF of 2 MHz due to the limited pulse energy provided by the fiber laser (only 270 nJ could be provided at the tissue surface) at this PRF.

3.2 Dynamic Imaging

To illustrate the dynamic imaging capability of the system, a mouse ear was imaged at a frame rate of 2 fps over a period of 32 s while being continuously translated laterally using a manual translation stage. The imaged area was 5 mm × 5 mm (500 × 2000 points), for which $N = 1$ million A-lines were acquired per frame while operating the fiber laser at a PRF of 2 MHz. Figure 4 shows three individual frames obtained at times $t = 0, 7$, and 13 s. The mouse ear was translated vertically in the x direction. To highlight the motion, a common blood vessel is indicated by a yellow arrow in each of the three frames in Fig. 4. A video can also be viewed online (Video 1), which illustrates the motion in real time. The repetitive accordion type image deformation observed in the video is
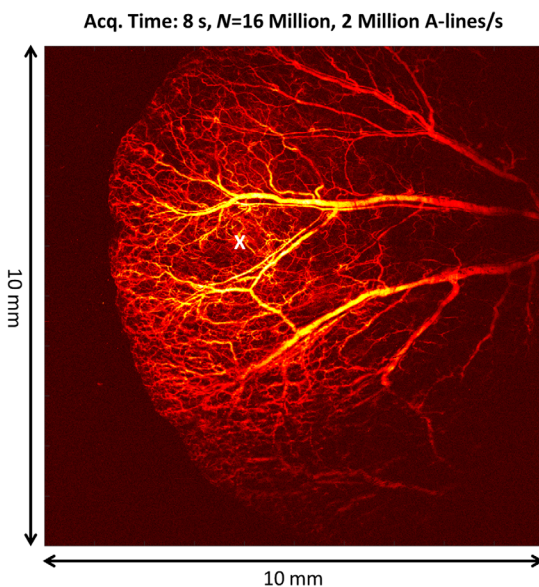
a consequence of insufficiently high frame rate and arises when the sample accelerates such that it moves an appreciable distance during the time taken to complete a single scan. The distortion is irregular and most pronounced at the start of each turn of the micrometer used to translate the stage as the sample is accelerating most rapidly at this time.

In a subsequent experiment, the mouse ear was imaged at a frame rate of 2 fps while remaining in a stationary position. The imaged area was 5 mm × 5 mm (500 × 500 points), for which $N = 0.25$ million A-lines were acquired per frame while operating the fiber laser at a PRF of 500 kHz. A total of 64 images were acquired at 2 fps with each image being represented as a single $\mathrm{MIP}_{\mathrm{pk-pk}}$. All 64 $\mathrm{MIP}_{\mathrm{pk-pk}}$ images were then combined to form a single 3-D dataset $(x, y,$ and $T)$, where T corresponds to the time at which each frame was acquired. A maximum intensity projection (denoted MIP_T) of this combined dataset was then formed by projecting the maximum values of the pixels lying along the temporal axis (T) on to the $x - y$ plane as shown in Fig. 5(a). In order to interpret this image, it is necessary to view video 2, which is available online. This video displays each of the 64 $\mathrm{MIP}_{\mathrm{pk-pk}}$ frames sequentially in time and appears to show red blood cells (RBCs) appearing and disappearing in successive frames. This is shown in Figs. 5(b) and 5(c), which show two successive individual frames of a small area of the scanned region indicated by the solid square box in Fig. 5(a). The white arrows highlight features that could be single RBCs, which are present in (b) but not in (c), whereas the yellow arrows highlight single RBCs which are present in (c) but not in (b). When an MIP_T through the temporal axis of the entire data set (i.e., all 64 frames) is formed, as shown in Fig. 5(d), a network of capillaries becomes visible. Although the images shown in Fig. 5 are likely to be broadly representative of the distribution of individual RBCs within the capillaries, the RBCs in any given single frame [e.g., see Figs. 5(b) and 5(c)] seem to be more sparsely distributed than expected. Moreover, inspection of Video 2 suggests their motion is somewhat discontinuous. These effects could be due to the relatively low SNR provided by single RBCs. Small random fluctuations in signal amplitude due to variations in the degree of overlap of the focussed laser spot with individual RBCs, pulse energy or RBC orientation may then cause the signal to randomly drop below the noise floor resulting in a sparser than expected contrast distribution as well as the perception of disorganised motion. By contrast, the larger microvessels do not exhibit these effects due to their high RBC density, which results in a higher SNR and a more continuous contrast distribution.

The video also shows transient variations in blood flow in larger vessels indicated in the video by arrows. To illustrate the flow in larger vessels in more detail, a second video (Video 3) was obtained at 2 fps when imaging a smaller area of 2.5 mm × 2.5 mm (500 × 500 points) with a smaller scanning step size of 5 μm. This area is delineated by the large dotted white box in Fig. 5(a) and the first frame of this video is shown in Fig. 6(a). The red and blue boxes show areas where variations in blood flow in specific vessels can be seen. Figure 6(b) shows individual frames of the region indicated by the blue box, taken at times $t = 10.5, 11.5$, and 12.5 s. Similarly, Fig. 6(c) shows individual frames of the region indicated by the red box, taken at times $t = 24.5, 26.5$, and 28 s. In both cases, the changes in contrast along the vessels are highlighted by an arrow, in each of the different frames. Videos of these two regions of interest are available online (Videos 4 and 5).

Acq. Time: 8 s, N=16 Million, 2 Million A-lines/s

Fig. 3 Photoacoustic image obtained *in vivo* of a mouse ear at 2 million A-lines/s. The scan area was 10 mm × 10 mm with a 2.5-μm step size and the total number of A-lines acquired was $N = 16$ million. The x and y galvanometers were driven at 250 and 0.0625 Hz, respectively. The PRF of the laser was 2 MHz and the pulse energy was 270 nJ. The position of the fiber sensor is indicated by the white cross and was 1.5 mm above the sample.

Frame rate: 2 frames per seconds, N⁰ of points: 1 Million, 2 Million A-lines per seconds
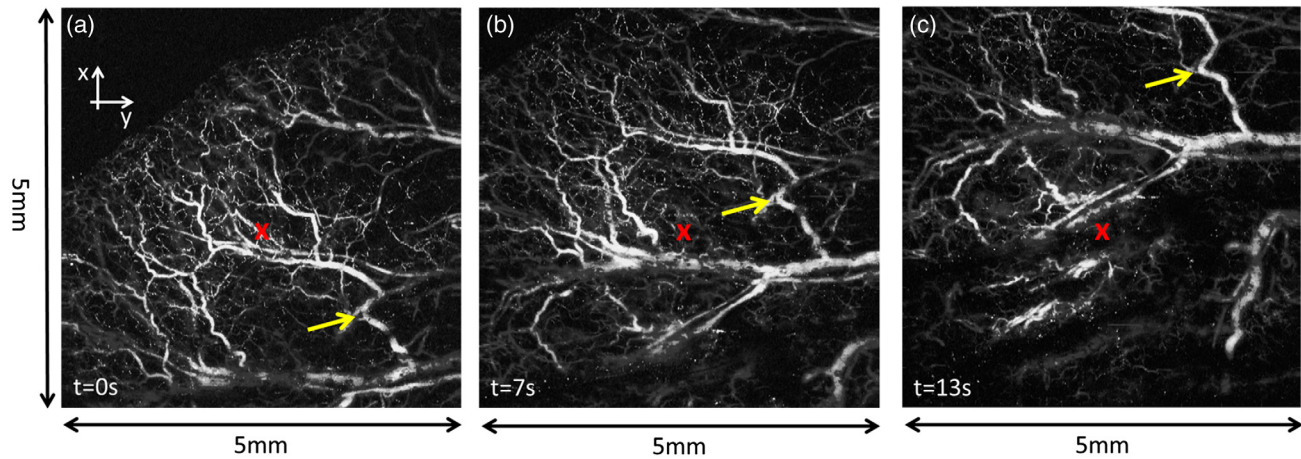

Fig. 4 Photoacoustic images of a mouse ear obtained at 2 fps while translating the mouse ear in the x direction. (a)–(c) Individual frames obtained at times $t = 0, 7$, and 13 s, respectively. A video can be viewed online (Video 1). The scan area was 5 mm × 5 mm with a 2.5- and 10-μm step size in the x and y directions, respectively, and the total number of A-lines acquired was $N = 1$ million per frame. The x and y galvanometers were driven at 500 and 1 Hz, respectively. The PRF of the laser was 2 MHz and the pulse energy was 270 nJ. The position of the fiber sensor is indicated by a red cross and was 1.5 mm from the sample. The yellow arrows indicate a common feature in each frame. (Video 1, MP4, 2 MB [URL: https://doi.org/10.1117/1.JBO.23.12.126502.1]).

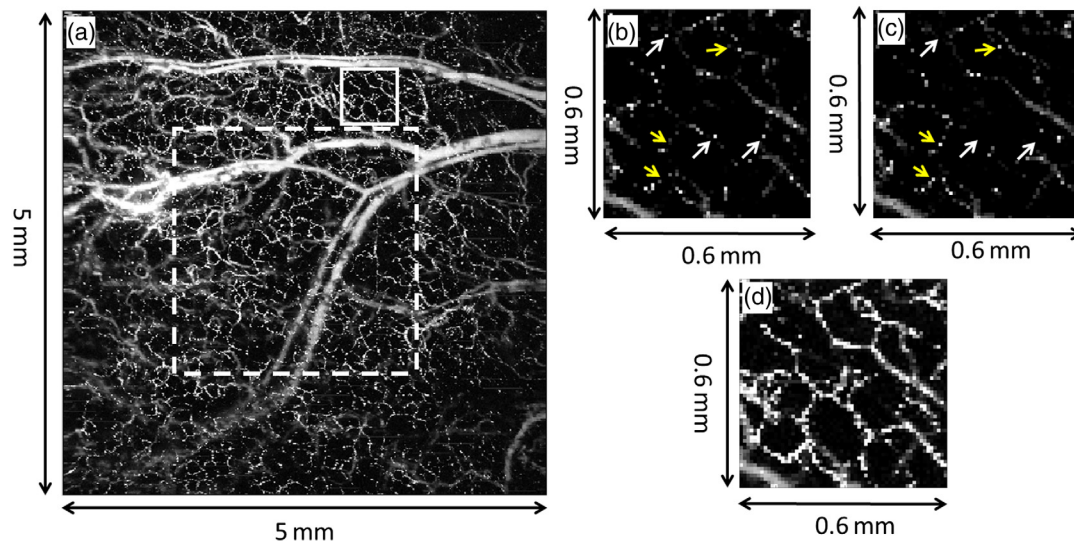**Frame rate: 2 fps, N = 250,000, 500,000 A-lines/s**

Fig. 5 Dynamic photoacoustic imaging of a large FOV showing the motion of single RBCs in the capillaries of a mouse ear imaged *in vivo* at a frame rate of 2 fps. A video can be viewed online (Video 2). (a) MIP_T through the temporal axis (T) of a single 3-D dataset (x, y, and T) formed from 64 successive MIP_{pk-pk} frames, where T corresponds to the time, in which each frame was acquired. (b) and (c) Two successive individual MIP_{pk-pk} frames of a region delineated in (a) by a solid square box. The white arrows highlight the presence of RBCs in (b) but not in (c) and the yellow arrows highlight the presence of RBCs in (c) but not in (b). (d) MIP_T through the temporal axis of the data set of the same region of interest as (b) and (c) shows delineation of capillaries vessels. The scan area of (a) was 5 mm × 5 mm with a 10-μm step size and the total number of A-lines acquired was $N = 250,000$. The x and y galvanometers were driven at 500 and 1 Hz, respectively. The PRF of the laser was 500 kHz and the pulse energy was 400 nJ. (Video 2, MP4, 2.4 MB [URL: https://doi.org/10.1117/1.JBO.23.12.126502.2]).

To demonstrate the possibility of obtaining higher frame rates than 2 fps, a mouse ear was imaged at a frame rate of 10 fps over an area of 1.25 mm × 1 mm (250 × 200 points) for a period of 32 s. The first frame of the dataset is shown in Fig. 7(a) and a video is available online (Video 6). Two

haemodynamic events appear in this dataset. The first one appears in the region delineated by a red box, which shows a region of low contrast flowing along a vessel. Figure 7(b) shows individual frames of this occurrence at times $t = 14.8$, 14.9, and 15 s, the region of low contrast being indicated by

Frame rate: 2 fps, *N*= 250,000, 500,000 A-lines/s
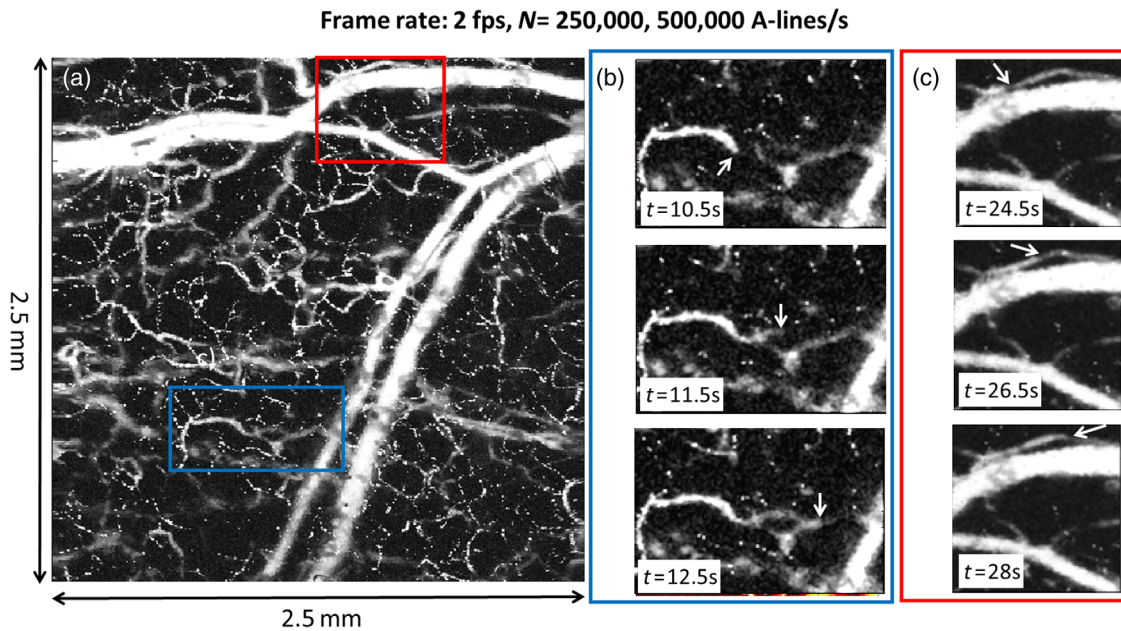

Fig. 6 Photoacoustic image obtained *in vivo* in a mouse ear at a frame rate of 2 fps showing variations in blood flow in selected regions. (a) The area delineated by the square dotted box in Fig. 5(a). A video can be viewed online (Video 3). (b) and (c) An expanded view of two areas of interest, where changes in blood flow in specific vessels (indicated by white arrows) are present, delineated in (a) by a solid red and a solid blue box, respectively. Videos can be viewed online (Videos 4 and 5). The scan area of (a) was 2.5 mm × 2.5 mm with a 5-μm step size and the total number of A-lines acquired was $N = 250,000$ per frame. The x and y galvanometers were driven at 500 and 1 Hz, respectively. The PRF of the laser was 500 kHz and the pulse energy was 400 nJ. (Video 3, MP4, 3 MB [URL: https://doi.org/10.1117/1.JBO.23.12.126502.3]); Video 4, MP4, 0.8 MB [URL: https://doi.org/10.1117/1.JBO.23.12.126502.4]); Video 5, MP4, 1.2 MB [URL: https://doi.org/10.1117/1.JBO.23.12.126502.5]).

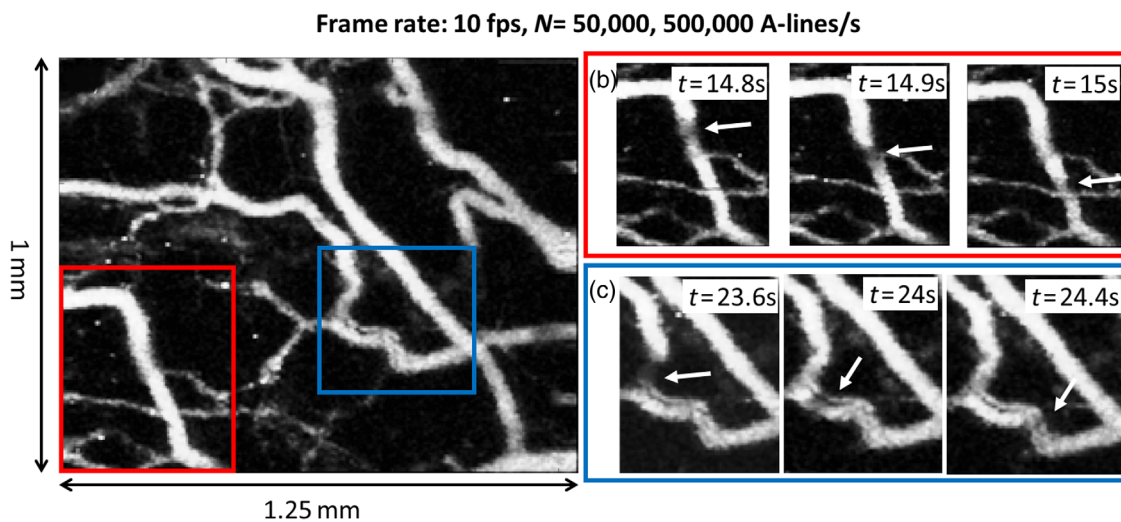**Frame rate: 10 fps, *N*= 50,000, 500,000 A-lines/s**

Fig. 7 Photoacoustic imaging of a mouse ear at 10 fps showing transient hemodynamic events in selected vessels. (a) Photoacoustic image obtained *in vivo* in a mouse ear at a frame rate of 10 images per second showing blood flow variations in two different vessels. A video can be viewed online (Video 6). (b) Individual frames obtained at times $t = 14.8$, 14.9, and 15 s of the region of interest delineated by the red box in (a). A video can also be viewed online (Video 7). (c) Individual frames obtained times $t = 23.6$, 24, and 24.4 s of the region of interest delineated the blue box in (a). A video can also be viewed online (Video 8). The scan area of (a) was 1 mm × 1.25 mm with a 5-μm step size and the total number of A-lines acquired was $N = 50,00$ per frame. The x and y galvanometers were driven at 1000 and 5 Hz, respectively. The PRF of the laser was 500 kHz and the pulse energy was 200 nJ. (Video 6, MPEG, 2.5 MB [URL: https://doi.org/10.1117/1.JBO.23.12.126502.6]); Video 7, MPEG, 0.24 MB [URL: https://doi.org/10.1117/1.JBO.23.12.126502.7]); Video 8, MPEG, 0.9 MB [URL: https://doi.org/10.1117/1.JBO.23.12.126502.8]).

an arrow. The second event appears in the region delineated by a blue box, and once again a region of low contrast can be seen flowing along a vessel. Figure 7(c) shows individual frames of this occurrence at time $t = 23.6$, 24, and 24.4 s, the region of low contrast being indicated by an arrow. Videos 7 and 8 show the complete time course of the events in Figs. 7(b) and 7(c).

4 Discussion and Conclusion

A laser scanning OR-PAM system based on a stationary fiber-optic ultrasound detector, an optimized galvanometer-based scanner, and a custom built high PRF fiber laser was developed. The large acoustic acceptance angle of the fiber-optic ultrasound detector enabled large FOVs to be imaged without requiring any mechanical scanning of the sample or sensor. This, in combination with the high scanning speed of the $x - y$ galvanometer, enabled the high PRF (2 MHz) of the fiber laser to be exploited in order to maximize imaging speed. The combination of these components enabled RA limited acquisition rates to be achieved for sub-mm OR-PAM, resulting in a factor of 4 faster acquisition than previously reported. For example, using a PRF of 2 MHz, the total acquisition time for an area as large as 10 mm × 10 mm over which 16 million A-lines were acquired was just 8 s. Scanning smaller areas can also enable real-time imaging. For example, images over a 1 mm × 1.25 mm FOV composed of 50,000 A-lines were acquired at 10 fps corresponding to 2000 B-scans per second. To our knowledge, a frame rate of 10 fps or higher with such a large FOV and number of A-line acquisitions is unprecedented. Higher frame rates can readily be achieved by reducing the scan area and number of A-lines; for example, a frame rate of 40 fps is achievable by scanning an area of 250 μm × 312.5 μm and acquiring 12,500 A-lines.

In this study, the OR-PAM imaging depth limit was taken as 750 μm, which corresponds to an RA limited PRF of 2 MHz. However, often the sample to be imaged will only be a few hundred of microns thick, and therefore, the PRF of the laser could be further increased, in order to accelerate the acquisition by a factor of 2 or 3. It may also be possible to further increase the imaging speed by surpassing the RA PRF limit. This could be achieved by exploiting the ability to arbitrarily control the temporal output of fiber lasers in order to implement coded excitation schemes in a similar manner to ultrasound imaging.[21,22] This flexibility could also be exploited in other ways. For example, arbitrary sequences of pulses could be used to investigate Grüneisen mediated effects[23] or measure blood oxygen saturation at a single wavelength by exploiting the different saturation intensities of oxy- and deoxyhemoglobin.[11] A tunable output can also be achieved with fiber lasers by exploiting the nonlinear effects exhibited by optical fibers such as stimulated Raman scattering[24,25] or supercontinuum generation in photonic crystal fibers.[6] Being able to generate a wide range of wavelengths would allow the spectroscopic identification and quantification of specific chromophores, e.g., to enable the measurement of blood oxygenation *in vivo*.[2]

Although the emphasis of this study is on acquisition speed, there is also scope to improve the lateral resolution. This could be achieved by reducing the lens focal length albeit at the cost of reduced FOV; previous laser scanning OR-PAM systems have demonstrated resolutions ranging from 3.5 μm for a 4-mm diameter FOV[26] to 0.5 μm for an FOV of <500-μm in diameter.[27] For the larger FOVs used in this study, it is conservatively estimated that the lateral resolution could be reduced to

<5 μm by replacing the current scan lens doublet with a custom-designed multielement telecentric lens.

In summary, a fast laser scanning OR-PAM system able to operate at RA limited acquisition rates was developed offering new opportunities for the rapid acquisition of large area, high-resolution images, and the real-time visualization of dynamic physiological events. Potential preclinical applications include studying hemodynamic responses, transient microcirculatory abnormalities, and contrast agent dynamics. The system may also find application for studying retinal conditions where high speed is required to avoid rapid eye motion.[28] In addition, a recent study has demonstrated the potential of OR-PAM imaging as a clinical tool for multilayered histology-like imaging,[29] which could be used intraoperatively to accurately assess tumor margins. However, this recent study required 70 h to image a sample (3 mm × 3.8 mm × 2 mm), which further highlights the need for high-speed OR-PAM imaging systems.

References

1. K. Maslov et al., "Optical-resolution photoacoustic microscopy for in vivo imaging of single capillaries," *Opt. Lett.* **33**, 929–931 (2008).
2. S. Hu, K. Maslov, and L. V. Wang, "Second-generation optical-resolution photoacoustic microscopy with improved sensitivity and speed," *Opt. Lett.* **36**, 1134–1136 (2011).
3. J. Yao and L. V. Wang, "Photoacoustic microscopy," *Laser Photonics Rev.* **7**, 758–778 (2013).
4. Z. Xie et al., "Laser-scanning optical-resolution photoacoustic microscopy," *Opt. Lett.* **34**, 1771–1773 (2009).
5. T. J. Allen, E. Zhang, and P. C. Beard, "Large-field-of-view laser-scanning OR-PAM using a fibre optic sensor," *Proc. SPIE* **9323**, 93230Z (2015).
6. M. Bondu et al., "High energy supercontinuum sources using tapered photonic crystal fibers for multispectral photoacoustic microscopy," *J. Biomed. Opt.* **21**, 061005 (2016).
7. W. Shi et al., "In vivo near-realtime volumetric optical-resolution photoacoustic microscopy using a high-repetition-rate nanosecond fiber-laser," *Opt. Express* **19**, 17143–17150 (2011).
8. W. Shi et al., "Optical resolution photoacoustic microscopy using novel high-repetition-rate passively Q-switched microchip and fiber lasers," *J. Biomed. Opt.* **15**, 056017 (2010).
9. W. Shi et al., "In vivo dynamic process imaging using real-time optical-resolution photoacoustic microscopy," *J. Biomed. Opt.* **18**, 026001 (2013).
10. H. Kang et al., "Real-time GPU-accelerated processing and volumetric display for wide-field laser-scanning optical-resolution photoacoustic microscopy," *Biomed. Opt. Express* **6**, 4650–4660 (2015).
11. J. Yao et al., "High-speed label-free functional photoacoustic microscopy of mouse brain in action," *Nat. Methods* **12**, 407–410 (2015).
12. E. Aytac-Kipergil et al., "Development of a fiber laser with independently adjustable properties for optical resolution photoacoustic microscopy," *Sci. Rep.* **6**, 38674 (2016).

13. Y. Liang et al., "2 MHz multi-wavelength pulsed laser for functional photoacoustic microscopy," *Opt. Lett.* **42**, 1452–1455 (2017).

14. T. J. Allen et al., "Large area laser scanning optical resolution photoacoustic microscopy using a fibre optic sensor," *Biomed. Opt. Express* **9**, 650–660 (2018).

15. T. J. Allen et al., "Novel fibre lasers as excitation sources for photoacoustic tomography and microscopy," *Proc. SPIE* **9708**, 97080W (2016).

16. J. A. Guggenheim et al., "Ultrasensitive Planoconcave optical microresonators for ultrasound sensing," *Nat. Photonics* **11**, 714–719 (2017).

17. E. Z. Zhang and P. C. Beard, "Characteristics of optimized fibre-optic ultrasound receivers for minimally invasive photoacoustic detection," *Proc. SPIE* **9323**, 932311 (2015).

18. J. Yao et al., "Wide-field fast-scanning photoacoustic microscopy based on a water-immersible MEMS scanning mirror," *J. Biomed. Opt.* **17**, 080505 (2012).

19. B. Dong et al., "Isometric multimodal photoacoustic microscopy based on optically transparent micro-ring ultrasonic detection," *Optica* **2**, 169–176 (2015).

20. G. Wissmeyer et al., "All-optical optoacoustic microscope based on wideband pulse interferometry," *Opt. Lett.* **41**, 1953–1956 (2016).

21. R. Y. Chiao and X. Hao, "Coded excitation for diagnostic ultrasound: a system developer's perspective," *IEEE Trans. Ultrason. Ferroelectr. Freq. Control* **52**, 160–170 (2005).

22. M. P. Mienkina et al., "Multispectral photoacoustic coded excitation imaging using unipolar orthogonal Golay codes," *Opt. Express* **18**, 9076–9087 (2010).

23. C. Tian et al., "Imaging and sensing based on dual-pulse nonlinear photoacoustic contrast: a preliminary study on fatty liver," *Opt. Lett.* **40**, 2253–2256 (2015).

24. P. Hajireza, A. Forbrich, and R. J. Zemp, "Multifocus optical-resolution photoacoustic microscopy using stimulated Raman scattering and chromatic aberration," *Opt. Lett.* **38**, 2711–2713 (2013).

25. L. Xu et al., "Raman-shifted wavelength-selectable pulsed fiber laser with high repetition rate and high pulse energy in the visible," *Opt. Express* **25**, 351–356 (2017).

26. B. Rao et al., "Hybrid-scanning optical-resolution photoacoustic microscopy for in vivo vasculature imaging," *Opt. Lett.* **35**, 1521–1523 (2010).

27. Y. Yuan, S. Yang, and D. Xing, "Optical-resolution photoacoustic microscopy based on two-dimensional scanning galvanometer," *Appl. Phys. Lett.* **100**, 023702 (2012).

28. Z. Hu et al., "Photoacoustic imaging in opthalmology," *Int. J. Ophthalmol. Eye Sci.* **3**, 126–132 (2014).

29. T. T. W. Wong et al., "Label-free automated three-dimensional imaging of whole organs by microtomy-assisted photoacoustic microscopy," *Nat. Commun.* **8**, 1386 (2017).

Biographies for the authors are not available.